Lab on a Chip

A high-throughput flow cytometry-on-CMOS for microwave-frequencies single-cell dielectric spectroscopy

Journal:	*Lab on a Chip*
Manuscript ID	LC-ART-03-2018-000299.R1
Article Type:	Paper
Date Submitted by the Author:	22-May-2018

Complete List of Authors:	Chien, Jun-Chau; University of California Berkeley, Electrical Engineering and Computer Science; Stanford University, Electrical Engineering Ameri, Ali; University of California Berkeley, Electrical Engineering and Computer Science Yeh, Erh-Chia; University of California Berkeley, Bioengineering Killilea, Alison; University of California Berkeley, Molecular and Cell Biology Anwar, Mekhail ; University of California, San Francisco, Radiation Oncology; University of California Berkeley, Electrical Engineering and Computer Science Niknejad, Ali; University of California Berkeley, Electrical Engineering and Computer Science

A high-throughput flow cytometry-on-CMOS for microwave-frequencies single-cell dielectric spectroscopy†

Jun-Chau Chien[a†], Ali Ameri[a], Erh-Chia Yeh[b††], Alison N Killilea[c], Mekhail Anwar[ad], and Ali M. Niknejad[a]

This work presents a microfluidics-integrated label-free flow cytometry-on-CMOS for the characterization of the cytoplasm dielectric property at microwave-frequencies. Compared with the MHz impedance cytometers, operating at GHz-frequencies offers direct intracellular permittivity probing due to electric fields penetrating through the cellular membrane. To overcome the detection challenges at high frequencies, the spectrometer employs on-chip oscillator-based sensors, which embedds simultaneous frequency generation, electrode excitation, and signal detection capability. By employing an injection-locking phase-detection technique, the spectrometer offers the state-of-the-art sensitivity, achieving less than 1 aF_{rms} capacitance detection limit (or 5 ppm in frequency-shift) at 100-kHz noise filtering bandwidth, enabling high throughput (> 1k cells/sec), with a measured cellular SNR of more than 28 dB. With CMOS/microfluidic co-design, we distribute four sensing channels at 6.5, 11, 17.5, and 30 GHz in an arrayed format whereas the frequencies are selected to center around the water relaxation frequency at 18 GHz. Issue in the integration of CMOS and microfluidics due to size mismatch is also addressed through introducing a cost-efficient epoxy-molding technique. With 3-D hydrodynamic-focusing microfluidics, we perform characterization on four different cell lines including two breast cell lines (MCF-10A and MDA-MB-231) and two leukocytes cell lines (K-562 and THP-1). After normalizing the higher frequency signals to the 6.5 GHz ones, the size-independent dielectric opacity shows differentiable distribution at 17.5 GHz between normal (0.905 ± 0.160, mean ± std.) and highly metastatic (1.033 ± 0.107) breast cells with $p << 0.001$.

Introduction

Label-free cell differentiation and sorting based on the physical properties intrinsic to the cells,[1–3] when comparing with the conventional labelling approaches such as fluorescent-activated cell sorting (FACS) or magnetic-activated cell sorting (MACS), offer the advantages of enhanced throughput, reduced reagent costs, and in particular, no alteration in the physiological functions of the cells, which is crucial for downstream molecular analysis or therapy usage.[4,5] Among all the label-free techniques,[3] microfluidics impedance cytometry has drawn great interests due to its hardware simplicity, ease of multi-modality integration, and the ability to monitor cellular changes.[6–14] Numerous applications including differential counting of leukocytes,[15,16] CD4/CD8 T-lymphocytes,[17] or CD64 neutrophils[18] from clinical blood samples have been demonstrated. Simultaneous electrical and mechanical phenotyping can also be carried out when coupling with constriction microfluidics.[19,20] A similar setup has also been adapted for large-scale studies on the electrical properties of the mouse tumor cells,[21] circulating tumor cells (CTCs),[22,23] and during stem cell differentiation.[24,25]

Most impedance cytometry have been focusing on measurement frequencies at kHz to MHz, quantifying only the cell sizes, specific membrane capacitances, cytoplasm conductivity, but not the molecular polarization inside the cells, where the latter can only be probed by increasing the measurement frequencies toward microwaves, and potentially into the millimetre-wave regime (1 ~ 100 GHz).[26,27] At these frequencies, we mainly measure the rotational polarization of the polar molecules, such as water, and its interaction with the surrounding micro-environment. (Fig. 1(a)). The quantity of interest is the complex permittivity ($\varepsilon = \varepsilon' - j\varepsilon''$) whose real and imaginary parts describe the amount of the energy stored and dissipated in a system under an electrical excitation, respectively. Similar to the low-frequency impedance spectra, the biological medium exhibits dispersive permittivity in the microwaves due to dielectric relaxation, as shown in Fig. 1(b), and is usually modeled using Debye and Cole-Cole equations as well as their variants.[28] As each cell exhibits differences in the water content, nucleus volumetric ratio, protein concentration, or cytoplasm irregularity, and other factors, we believe that the cellular permittivity measured at high frequencies can be used to enhance the resolution in label-free discrimination between different cells. Therefore, this paper aims to develop a platform for characterizing these microwave fingerprints (Fig. 1(b)) by measuring the dielectric contrast between cells and the hosting medium.

Several works have attempted GHz measurements at the cellular levels. Grenier et. al.[29] first demonstrated broadband (0.4 – 35 GHz) measurements of large number of suspended cells on top of a coplanar waveguide (CPW) transmission lines using vector network analyser (VNA); later on, the same group advanced toward single-cell measurements to account for heterogeneity by equipping the sensor with microfluidics mechanical traps, and demonstrated correlated changes in the microwave property of the cells under different stimulus such as heating or electroporation.[30–32] Ning et. al.[33] employs similar strategy using dielectrophoresis (DEP) for single-cell trapping. Yang et. al.[34] enhances the sensing sensitivity with interferometry at 5 GHz and shows differentiation capability between viable and non-viable yeast cells. It is worth highlighting the work from Zhang et. al[35], though at a smaller scale, shows noticeable differences between colorectal cancer

[a] *Department of Electrical Engineering and Computer Science, University of California at Berkeley, Berkeley, CA 94720, United States;* [†] *Jun-Chau Chien is currently at Department of Electrical Engineering, Stanford University. E-mail: jcchien@berkeley.edu and niknejad@berkeley.edu*
[b] *Department of Bioengineering, University of California at Berkeley, Berkeley, CA 94720, United States;* [††] *Erh-Chia Yeh is currently with mFluidx Inc.*
[c] *Department of Molecular and Cell Biology, University of California at Berkeley, Berkeley, CA 94720, United States*
[d] *Department of Radiation Oncology, University of California at San Francisco, San Francisco, CA 94158, United States*
†Electronic Supplementary Information (ESI) available.

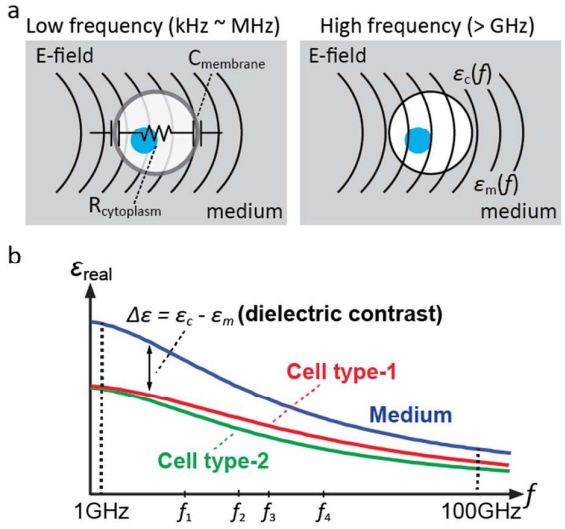

Fig. 1 (a) Conceptual illustration of the electric field (E-field) distribution across a single cell suspended in the medium at low and microwave frequencies. Increasing the operating frequencies toward GHz enables non-invasive intra-cellular access by bypassing the low-impedance membrane. At MHz, E-field partially penetrates through the membrane. This enables the quantification of both the specific membrane capacitance and the cytoplasm conductivity. At GHz, the cell and the medium are modelled as material with permittivity ε_c and ε_m, both a function of excitation frequency. (b) This work characterizes single-cell dielectric spectroscopy at microwave frequencies as fingerprints for label-free discrimination. Only the real part of the permittivity is measured. As cells are suspended in the medium, the actual measurement reflects the dielectric contrast ($\Delta\varepsilon = \varepsilon_c - \varepsilon_m$) against the background medium. Measurements are performed at four frequencies (6.5, 11, 17.5, and 30 GHz).

cells at different cancer stages. There, a series of MEMS-fabricated LC-based resonators spanning from 5 to 14 GHz is measured using VNA. The main bottleneck of this work lies in its measurement complexity and the labor-intensive protocols, requiring cell immobilization, culture medium evaporation (to enhance signal contrast), and computation-intensive forward modeling. Consequently, limited throughput (< 1 cell/min) and accuracy make single-cell fingerprints over a broad frequency ranges not yet attainable.

Single-cell measurement at GHz frequencies poses three main challenges. First, the measurement sensitivity is limited even with bench-top high-performance VNAs. This is simply because of the presence of directional couplers and switches at the instrument front-end for splitting and directing the guided waves. The high loss from these passive microwave components can degrade the noise figure of the receiver as much as > 20 dB (estimated based on the noise floor and filtering bandwidth provided by the technical data sheet of KeySight N5242 4-port PNA). The noise floor is further elevated due to interconnecting cables and high-frequency probes (a dB extra loss is a dB increase in the noise figure). Second, water molecules are highly absorbent to the microwave energy, which degrades the signal-to-noise ratio (SNR). Loss tangent ($\tan\delta = \varepsilon''/\varepsilon'$) can be as high as 1 in the biological medium around the water relaxation frequency (~18 GHz). This also reduces the benefit of using resonator-based sensor where loaded quality-factor (Q) will be significantly degraded. For example, a resonance-enhanced impedance flow cytometry at 89 MHz presented in Haandbæk et. al.[36] fails to achieve adequate sensitivity at normal medium ionic strength (solution conductivity ≈ 1.5 S/m). Third, the accuracy in cellular parameter extraction is highly dependent on the quality and the complexity of the system calibration. Complex multi-step multi-structure calibration is often necessary for such purpose.[37]

To circumvent instrumentation limitation, custom sensor design for GHz dielectric measurements using silicon-based technologies, such as CMOS and SiGe processes, offer a new degree of freedom in system innovation and optimization as well as form factor miniaturization.[38–45] However, previous works in this domain have been mostly limited with liquid measurements capability at relatively large sensing volume (hundreds of nL) or suffered from insufficient sensitivity for single-cell dielectric spectroscopy. As an example, Mohammad et. al.[46] presents a 1.4-GHz CMOS dielectric sensor, which offers a 14-aF capacitive resolution at a 100-msec averaging time yet sub-aF is necessary to resolve 5% change in cytoplasm permittivity with > 20 dB SNR (details will be discussed in the next section). On the other hand, Ferrier et. al.[47,48] implements a state-of-the-art 1.5-GHz near-field sensor using discrete electronics, and achieves 0.65-aF sensitivity at 10-msec system response time; however, the system is tailored for displacement measurements in a microfluidic dielectrophoresis (DEP) cytometry at lower throughput.

To address the aforementioned three challenges, this paper presents a microwave spectrometer for high-throughput flow cytometry in a CMOS/Microfluidics assembly and takes advantage of technology co-integration for reduced parasitics and enhanced sensitivity. Our sensing elements are an array of on-chip LC-based oscillators, which offers the capability for simultaneous frequency generation, electrode excitation, and signal detection, tuned to different frequencies. By further employing injection-locking technique and phase-sensitive readout architecture,[49,50] we push the sensitivity limits toward 1 aF_{rms} at 100-kHz noise filtering bandwidth (5 ppm in frequency-shift). This level of sensitivity offers the capability for detecting < 0.5% change in the cellular permittivity at limit-of-detection (LoD).

In addition to the advancement in the electronics, we also address the integration issue at the CMOS/microfluidics interface. Due to size mismatch, conventional CMOS/microfluidic packaging either requires multiple steps of lithography-based post-processing[51–58] or is not equipped with the capability for more complex fluidic functionalities other than sample delivery.[59–61] Recent works[62,63] have taken advantage of 3-D microfluidics to perform hydrodynamic focusing on top of the CMOS chip; however, they require high-quality vertical fluidic channel formation and precise alignment, pushing the design complexity toward microfluidics. On the other hand, Zheng et. al.[64] presents a non-standard flexible packaging using PDMS with liquid-based metallic interconnections. To overcome such a size-mismatch issue, we present a highly modular methodology that employs (1) a

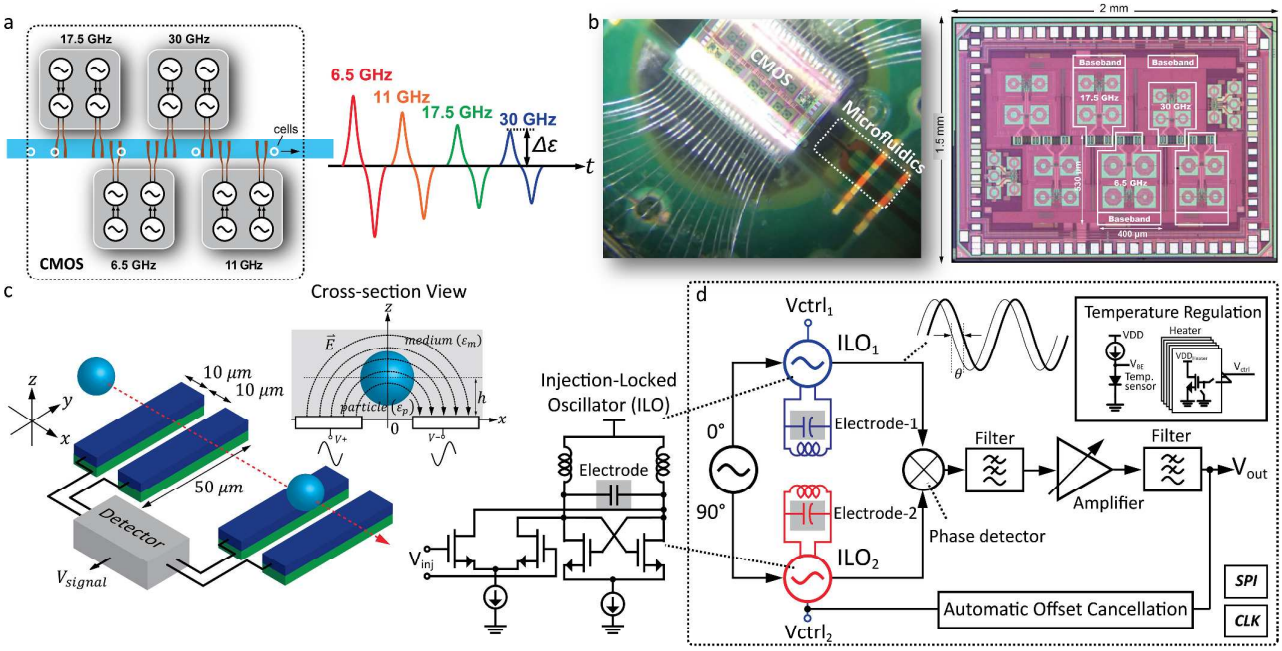

Fig. 2 (a) CMOS spectrometer with distributed sensor array architecture. Each sensing channel consists of two co-planar electrodes performing sequential-difference measurements. Four bipolar waveforms are registered as a cell flow through. The pulse height is proportional to the cellular dielectric contrast (Δε) against the hosting medium. The electrodes from each sensing channel are aligned at the center of the chip to interface with the microfluidic channel. The elevation of the flowing cells from the electrode is controlled by a 3-D hydrodynamic focusing microfluidics. (b) Device photo with microfluidics (colored with blue and red food ink) on top of the CMOS and the chip micrograph of the CMOS spectrometer. Four channels (highlighted) are used where the other two are for testing purpose. (c) The illustration of a single sensing channel. The electrode parameters are l = 50μm, w = 10μm, and g = 10μm. (d) The system block diagram of the readout channel. It consists of two injection-locked oscillator sensors in interferometry configuration. Each ILO drives a pair of electrodes. Perturbation in the ILO oscillation frequencies is transduced to phase shift and detected using a mixer-based phase detector. Peripheral circuits include automatic offset cancellation, temperature regulation, serial-to-parallel interface (SPI), and on-chip clock (CLK) and bias generation.

simple CMOS-in-PCB packaging, which takes only two steps of injection molding for surface planarization and bond-wire encapsulation, and (2) a 3-D printed PDMS-molded microfluidic chips demonstrating 3-D hydrodynamic focusing. A unique feature of our approach is the large microfluidic working area for accommodating different fluidic functions. This enables the realization of future "lab-on-CMOS" devices.

As fluids flow directly on top of the CMOS electronics, the system stability can potentially be compromised. To ensure highest possible accuracy, our design includes both the temperature regulation as well as automatic offset/drift cancellation. We also introduce background calibration during the flow measurements, in which polystyrene beads are exploited as a material reference in our cell line experiments for highest possible repeatability. We will present single-cell dielectric spectroscopy measurements from four different cell lines as comparisons.

Materials and methods

Sensing principle

The dielectric property of each individual cell is detected through a fringing electric fields generated by on-chip co-planar electrodes. At microwave frequencies, the induced capacitance change is proportional to the dielectric contrast between the cells and the surrounding medium, as described by the Clausius-Mossotti factor, K_{CM}:[48]

$$K_{CM} = \frac{\varepsilon_c(\omega) - \varepsilon_m(\omega)}{\varepsilon_c(\omega) + 2\varepsilon_m(\omega)} \approx \frac{1}{3}\frac{\Delta\varepsilon(\omega)}{\varepsilon_m(\omega)} \quad (1)$$

where ε_m and ε_c are the permittivity of the medium and the cell, respectively, ω (= $2\pi f$) is the measurement frequency, and cells are assumed perfect spheres with radius a. The approximation is applicable when the change in the permittivity is small compared to its background, which is the case when measuring the cells in the culture medium (but not for polystyrene beads). Due to the near-field operation, the capacitance change induced by a flowing cell is derived based on energy perturbation theory with quasi-static approximation as:[48,49]

$$\Delta C = 4\pi\varepsilon_m a^3 \mathrm{Re}\{K_{CM}\}\frac{|E_0|^2}{V_0^2}, \quad (2)$$

where $|E_0/V_0|$ is the normalized electric field intensity experienced by the cells, and is assumed uniform across the space. From Eq. (2), we can calculate the sensor must resolve less than 10 aF of capacitance change with adequate signal-to-noise ratio (SNR) when differentiating two different cells of equal size (10 μm in diameter) but 5% difference in their permittivity ($\Delta\varepsilon_p/\varepsilon_p$ = 2/40 at ε_m = 60) given a normalized field intensity of 5×10^4 V/m. Achieving this level of sensitivity at high bandwidth is therefore the main challenge

in our spectrometer design. The measured signal is also a function of the cellular size and the field intensity whereas the latter is a function of the elevation of the cell with respect to the electrodes; therefore careful calibration is mandatory to ensure meaningful interpretation and will be discussed in the Results and Discussion section. Finally, it is worth emphasizing that we focus on measuring only the capacitance change (ε') but not the associated cellular losses (ε''). This is feasible as the real and the imaginary parts of the permittivity follow Kronig-Kramers relation and form a Hilbert Transform pair.

Sensing System

Array-based spectrometer. Unlike the conventional spectrometer where a broadband transceiver is used to drive and detect the minute change of the microwave signal, our CMOS spectrometer instead consists of several narrowband sensing elements distributed in line with a straight microfluidic channel hosting the flowing cells (Fig. 2(a) and Fig. 2(b)). Such a distributed scheme enables not only the sensitivity optimization in each individual sensing channel but also broadband single-cell characterization without employing cell trapping. Furthermore, close integration of electrodes and readout circuits in CMOS technology minimizes signal degradation due to lengthy interconnections and the power consumption (~16 mW/channel). This is an essential step toward battery-powered and portable bio-assays and cytometry. We have chosen four measurement frequencies centered around the relaxation frequency of the water molecules (18 GHz), spanning from 6.5 to 30 GHz. Each electronic channel consists of two pairs of coplanar electrodes (Fig. 2(c)). Therefore, a single flowing cell will register four bipolar pulses due to sequential difference sensing (Fig 2(a)). This strategy not only improves the SNR by 3 dB but also achieves better drift mitigation by having one pair of electrodes serve as the reference for the other. The pulse height is proportional to the dielectric contrast whereas the time distance between the two peaks infers the flow velocity. Additional channels can be included with more silicon real estate.

Sensing elements. We implement the sensing co-planar electrodes using the metallization layers from CMOS back-end. It consists of a parallel combination of a copper layer (M9) and an aluminium pad layer. The passivation is removed by the foundry to preserve the electrode sensitivity. The electrode pair has a dimension of 10 μm × 50 μm with a pitch of 20 μm. The pitch is selected to match the diameter of the cells as a balance between the field intensity and the fringing distance. As the electrode length is relatively short compared to the wavelength ($\lambda \approx 5$ mm at 30 GHz for transmission lines with the SiO_2 substrate), the field distribution due to the standing-wave effect is negligible, making the signal amplitude insensitive to the location of the cells when flowing across the electrodes. This greatly relaxes the precision requirement in microfluidic focusing.

Readout architecture. To boost the sensitivity, we resonate the electrode capacitance with an on-chip spiral inductor. The cells-induced capacitance change is measured through the shift in the resonance frequency with a boosting factor proportional to the quality factor (Q), of the LC-tank. Moreover, the resonator is coupled with active transistors to form an LC-oscillator, performing simultaneous microwave signal generation, electrodes excitation, and cellular sensing. Unlike the conventional frequency-shift detection scheme using frequency counters,[65] we injection lock the sensing oscillators (injection-locked oscillator, ILO) with a master source at a similar frequency. Injection locking ensures that the frequencies of the two sensing oscillators (ILO_1 and ILO_2 in Fig. 2(d)) remain identical to that of the input source, transducing the perturbation in their resonance frequencies into phase shifts (detailed description of the operation are provided in Fig. S1 in ESI). The amount of phase shift can be related to the frequency changes by:

$$\theta \approx 2Q \frac{I_{osc}}{I_{inj}} \frac{\Delta\omega}{\omega_0}, \quad (3)$$

where Q is the quality factor of the resonator, I_{osc} and I_{inj} are the oscillation and the injection currents, respectively. In comparison to a passive resonator, the ILO offers extra gain boosting factor proportional to the ratio between I_{osc} and I_{inj}. This electronically-tunable transduction gain maximizes the sensitivity of the sensing oscillators and hence the limit of detection. Fig. 2(d) exhibits the electronic readout block diagram. A mixer-based phase detector performs both the frequency conversion from the microwave frequency to DC as well as the phase detection. The master source is generated using an on-chip free-running quadrature-phase voltage-controlled oscillator (QVCO) where its noise is self-canceled at the detector output due to interferometry. After filtering by a 1st-order RC filter to eliminate the 2nd harmonic ($2\omega_0$), the signal is amplified and digitized through an on-chip variable gain amplifier (VGA) and an analog-to-digital converter (ADC). Chopper stabilization is also employed to mitigate flicker-noise induced low-frequency drift (Fig. S2). From our electrical characterization, our 30-GHz sensor measures < 1 aF_{rms} of resolution at 100-kHz noise filtering bandwidth when the electrodes are immersed in water with an estimated loaded Q-factor of 3. Benefiting from the high sensitivity, our cytometer demonstrates high-throughput capability (> 1 kcells/sec, limited by microfluidics and its controls). Due to fast flow rate, high-frequency excitation (> 6GHz), and low oscillation amplitude (0.6-V_{amp} differentially), the effect of electroporation is minimal. It worth mentioning that such a high resolution outperforms those using high-performance VNA[30] or off-the-shelf discrete components.[47] The former achieves 10 aF_{rms} resolution whereas the latter offers 0.65 aF_{rms} with 50-Hz noise filtering bandwidth.

Our integrated circuit is designed and fabricated in 65-nm CMOS technology by Taiwan Semiconductor Manufacturing Company (TSMC). Computer-aided design (CAD) simulators including SpectreRF® (Cadence Design Systems), HFSS™ (Ansys Inc.), EMX® (Integrand Software Inc.), and COMSOL Multiphysics® are used for design and simulations of the circuits, CMOS/microfluidic interface, fluidic dynamics, and on-chip microwave components.

Drift cancellation and data acquisition. To mitigate sensor drift, negative feedback loops that track temperature and offset variations are included. The temperature regulation and automatic offset/drift tracking loops are closed off-chip using surface-mount operational amplifiers (OPAMP), capacitors, and resistors. Detailed system parameters are provided in Fig. S3. Note that these functions can be

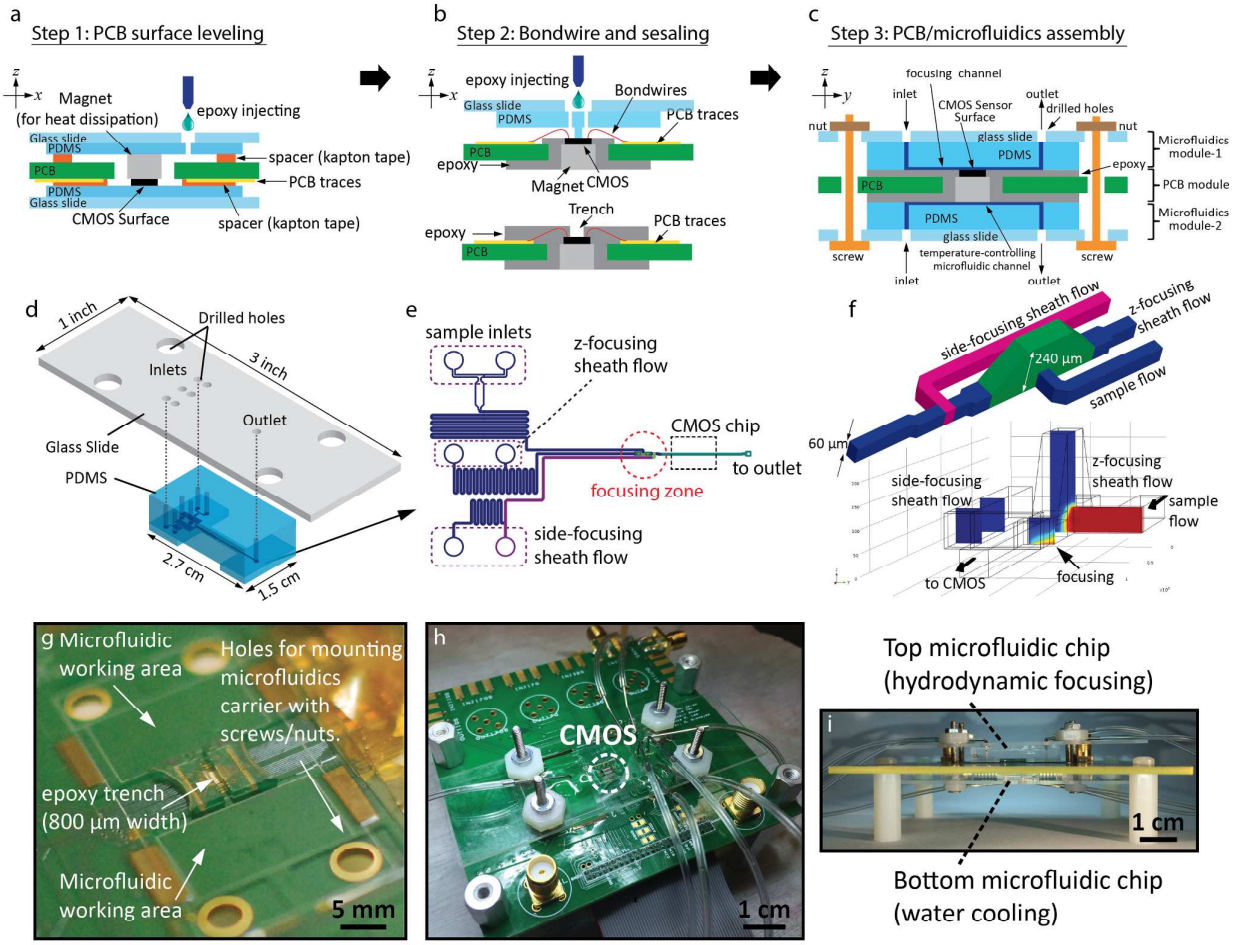

Fig. 3 Modular CMOS/microfluidic integration procedure. (a) In step 1, PCB surface is elevated with respect to the CMOS using epoxy. Kapton tape protects the PCB bond pads and serve as spacers with adjustable thickness. A magnet is mounted at the backside of the CMOS to enable microfluidic cooling. (b) In step 2, the spacers are removed, and the chip pads are wire bonded to the PCB traces. The bond-wires are sealed using the same type of epoxy. During epoxy application, the CMOS electrodes are protected using a temporary PDMS mold. (c) In step 3, two microfluidics are aligned under a microscope and tightened mechanically against the PCB/CMOS module using screws and nuts. The bottom cooling microfluidics needs no precise alignment. (d) The illustration of the microfluidics module. It consists of a 3D-channel-patterned PDMS mounted on a glass carrier with through holes for liquid interconnects. We utilize stereolithography technology to implement the master mold for PDMS casting. (e) Details of the microfluidic design for 3-D hydrodynamic focusing. It consists of a sample flow and two sheath flows. Each flow has two inlets differed by the hydrodynamic resistance. (f) A zoom-in view of the 3-D hydrodynamic focusing section. COMSOL simulation results demonstrating the profile of the sheath and the sample flow under a ratio of 8:1. (g) The photo of the CMOS/PCB module. A trench formed by the bondwires-sealing epoxy is used to host the PDMS for interfacing CMOS chip. Our device includes a large microfluidics working area on both sides of the CMOS chip. This enables the addition of extra fluidic functionality such as sample preparation. (h) The assembled device photo. (i) The cross-section view of the device with dual microfluidics sandwiching the PCB module.

integrated into the same CMOS chip to further miniaturize the system.

The CMOS spectrometer is digitally controlled using Opal Kelly XEM3001 Xilinx Spartan-3 FPGA for gain programming, offset cancellation, and frequency calibration. A system photo is shown in Fig. S4. Instead of using on-chip ADC, we digitize the cytometry data using Tektronix DPO4054, which is equipped with 2 GB of storage. The acquired data is transferred to a personal computer for further analysis in Matlab (Mathworks).

CMOS/Microfluidics

Our CMOS/microfluidics assembly consists of two modules: a CMOS/PCB module and a 3-D hydrodynamic-focusing microfluidic chip. Both are mechanically assembled without permanent bonding, thus maximizing the flexibility through CMOS/PCB re-use for testing different microfluidic designs. Next, detailed processing steps are described.

CMOS/PCB module. First, we coated the bare CMOS dies with 50-nm silicon nitride using PECVD (Plasmalab 80plus, Oxford Instrument) at 200°C and an RF power of 22.5 W. The deposition rate is 20 nm/min. This protects the Al electrodes from electrolysis due to the existence of supply voltage (1.0V) at the cost of 20% reduction in the field intensity. Experiments show no degradation in the signal amplitude in the measured polystyrene beads after a few months of fluidic testing. On the contrary, the uncoated electrodes corrode promptly within the first three hours of fluidic testing, as

shown in Fig. S5. After nitride deposition, CMOS bond pads are re-exposed using reactive ion etching (REI, Plasma Equipment Technical Service Inc.) with O_2 and CF_4 mixture at an RF power of 150 W under 120 mTorr. The CMOS sensing electrodes are protected through a piece of PDMS slab during etching (Fig. S6). The etch rate at this power level is 1.9 nm/sec.

Next, a 1/16"-diameter cylinder-shaped ~~metallic object, here using~~ neodymium magnet (K&J Magnetic, Inc) is mounted on the backside of the CMOS die using silver epoxy for heat dissipation. Here we choose the magnet due to its size matching to the CMOS chip and the PCB cavity, as described later, and its commercial availability, but any metallic object should serve well. The CMOS/magnet is then encapsulated inside a 3-mm diameter through-hole centered at the PCB using a bio-compatible epoxy (302-3M, Epo-Tek), as shown in Fig. 3(a). In this step, we mount multiple layers of kapton tape, with total thickness around 300 μm, on the PCB to protect the bonding pads from epoxy coverage. Importantly, these kapton tapes also serve as a spacer for the flowing epoxy. Prior to epoxy injection, the device is brought in contact with a slab of cured PDMS (Fig. 3(a)). Mechanical pressure is applied using clamps to prevent air gaps and epoxy flowing over the CMOS surface. After epoxy curing (3 hours in 90°C oven or 24 hours under room temperature), the kapton tape is removed manually and the CMOS chip is wire bonded to the PCB using 1-mil diameter aluminium wires (Fig. S7). These bond-wires are then sealed with the same epoxy under room temperature. During this last step, the surface of the CMOS chip is protected using a cured PDMS to create an 800-μm wide trench for hosting the microfluidic module (Fig. 3(b)).

As shown in Fig. 3(c) and Fig. 3(g), the epoxy filling technique enables large microfluidic working area directly on the PCB. This facilitates the integration of different fluidic functionalities on the same substrate. In this work, we customize the fluidic resistances in each channel by designing different channel lengths and widths. It is worth mentioning that no surface treatment is applied in each of the steps as we did not observe any adhesion between PDMS, epoxy, PCB, and the kapton tape.

Microfluidics module. The microfluidic prototyping device consists of a patterned PDMS (Sylgard®184, Downing, ratio 10:1) bonded to a glass carrier using oxygen plasma (15 sec under 60 W of RF power at 120 mTorr), as illustrated in Fig. 3(d). The master mold is fabricated using 3-D printing stereolithography (MicroFine Green Resin, ProtoLabs) offering a resolution of 40 μm in both lateral and vertical dimensions (Fig. S8). Experiments showed that PDMS can be easily peeled off from the 3-D printing resin and therefore no silanization is applied before PDMS casting. For fluidic interconnections, the through holes on the glass carrier are created manually using diamond drills. Stainless steel blunt needle and tygon tubing are used for fluidic connection to syringe pumps (Fusion 100, Chemyx Inc.). The microfluidics module and the CMOS-embedded PCB are aligned under a microscope and assembled manually using mechanical screws (Fig. 3(c)). On the bottom side of the PCB, a single channel microfluidic chip interfaces the heat-distribution magnet mounted on the backside of the CMOS die, for temperature control. Fig. 3(e) illustrates the layout of the microfluidic channels. Fig. 3(h) and Fig. 3(i) depict the device photo.

3-D hydrodynamic focusing microfluidics. To ensure single-cell flow with consistent position and elevation inside the microfluidic channel, we employ the 3-D hydrodynamic focusing technique in our microfluidic design. As shown in Fig. 3(f), after the sample channel intersecting with the first sheath flow at the 3D junction, a stepping down of the channel height from 240 to 60 μm focuses the cells toward the floor of the fluidic channel.[66,67] Followed by the second sheath flow coming from the side, the cells are focused to the bottom left corner of the fluidic channel. Fig. 3(f) also shows the COMSOL FEM simulation using mass transport module. The simulation shows a flow-rate ratio of 8× between the sample and the first sheath flow confines the sample stream within ~ 20 μm away from the bottom of the fluidic channel. The flow rate of the second sheath flow is kept identical to that of the first one.

Sample Preparation

Mammalian cells, purchased from ATCC and additionally mycoplasma tested and authenticated by short tandem repeat profiling, were cultured at 37°C with 5% CO2 in 10cm tissue culture treated plastic dishes. MCF-10A human mammary epithelial cells were maintained in DMEM-F12 supplemented with 5% horse serum (purchased from VWR), 20ng/ml epidermal growth factor, 0.5μg/ml hydrocortisone, 100ng/ml cholera toxin and 10μg/ml insulin (Sigma). MDA-MB-231 human mammary epithelial carcinoma cells were maintained in DMEM glutamax with 10% FBS. THP-1 human monocyte cells were maintained in RPMI-1640 supplemented with 10% FBS, 1% sodium pyruvate, 10mM HEPES, 4.5gm/L glucose, 0.05mM beta-mercaptoethanol (BME). K562 leukemic cells were maintained in RPMI1640, 15% FBS, 1% sodium pyruvate, 10mM HEPES. All other cell culture-certified supplies were obtained from Thermo Fisher Scientific.

Prior to the experiments, adherent cells were detached with 0.25% or 0.05% trypsin-EDTA, inactivated with media containing serum and diluted with isotonic buffer. Suspension cells were diluted directly into an isotonic buffer for measurements. A Beckman Z2 Coulter counter was used to obtain cell concentration, mean, median and standard deviation (Table S1). To avoid microfluidic channel blockage, both the cells and the polystyrene beads with a diameter larger than 6 μm (Polyscience Inc.) are flushed through CellTrics® filters (Sysmex America Inc.) to avoid large debris. Syringe filters with 0.7- and 1.2-μm pore sizes (Scientific Equipment of Houston) are used for smaller beads with a diameter of 0.5 and 1.0 μm. Both the samples and the sheath flows are delivered to the microfluidics using syringe pumps. Each cellular experiment is completed within one hour at room temperature. Between each batch of measurement, we rinse the fluidic channel with bleach (Bleach-Rite, Current Technologies Inc.) at a high flow rate for 15 minutes followed by DI-water without disassembling the microfluidics. It is found that bleach is effective in removing the residues and debris formed on top of CMOS surface without affecting the electrode integrity and the corresponding sensitivity, as confirmed by the repeatability measurements (Fig. S9 and Table S2).

Results and discussions

System calibration and validation

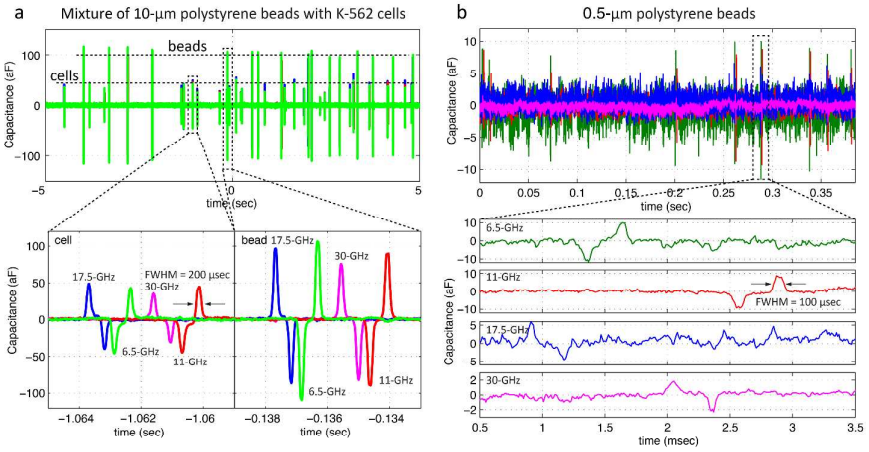

Fig. 4 (a) Measured four-channel time-domain signals from a mixture of 10-µm polystyrene beads and K-562 cells. Beads and cells are readily differentiable based on pulse height. The full width at half maximum (FHWM) of each pulse is ~200 µsec. (b) Measurements of 0.5-µm polystyrene beads. The FWHM is reduced to < 100 µsec due to enhanced flow rate.

To minimize batch-to-batch variation, both foreground and background calibration are included in each batch of cell line measurements (detailed steps are presented in ESI, Fig. S10). In short, we first calibrate the sensitivity as well as the nonlinearity in the CMOS electronics (foreground calibration, Fig. S11). Second, we conduct two sequential measurements for each type of cells: (1) cells/beads mixture and (2) cells-only measurements. This scheme allows the compensation of the channel-to-channel and chip-to-chip variation in the electrode sensitivity (due to thickness variation in its nitride coating and electrode aging) with polystyrene beads serving as a material reference (background calibration). Post-processing for the correction is described in Fig. S12. Third, the permittivity of the cell-free culture medium (filtered using a membrane with 0.2-µm pore size) is extracted using reference liquids with known permittivity (Fig. S13), and the averaged cytoplasm permittivity can be calculated using Eq. (1).

We validate our system using polystyrene beads (Polysciences, Inc.) in several steps. First, we measure and quantify the signal distribution of the 5.8-µm diameter polystyrene beads from two batches with different coefficients of variation (CV) (σ_1/m_1 = 0.447µm/5.801µm and σ_2/m_2 = 0.232µm/5.85µm). The measured histograms, averaged over four frequency channels, give distributions (23.93% and 13.3%) that are in close agreement with the volumetric variation calculated from the vendor-provided data (24.94% and 12.37%) (Fig. S14). In addition, Fig. S14 shows that no significant change has been observed in the bead distribution over the four sensing channels, which are separated at a distance of 1 mm. This indicates stable control of the cellular elevation in the fluidic channel is effective with our hydrodynamic focusing. Next, the repeatability of the system with the bleach-cleaning protocol is tested by comparing the mean absolute capacitance value from two consecutive bead measurements in the culture medium. Table S2 shows that our system presents a repeatability error of 2%. As this error is much smaller than the measured CV from all the cell lines (~25%), we consider this to be acceptable. Third, we perform mixture measurements on 6- and 10-µm beads and verify that the ratio between the two signals is in agreement with the volumetric ratio (Fig. S15). This indicates that the 3-D hydrodynamic focusing can confine two different particle sizes at similar elevation height. This is important as we are mixing 10-µm beads with cells (> 13 µm) for background calibration.

Fig. 4(a) shows an example of captured waveforms measured from a mixture of 10-µm polystyrene beads and K-562 cells (diameter 14.9 ± 1.9 µm). It is clearly seen that the polystyrene beads exhibit significantly larger signals compared with the cells though its diameter is only two third of the cells. This is due to the high dielectric contrast of the polystyrene matrix ($\varepsilon_{polystyrene}$ ~ 2.2) in the culture medium (ε_{medium} ~ 60 at GHz). The flowing velocity in these measurements is approximately 150 mm/sec calculated from the time difference between the two bipolar peaks. The velocity is limited by the focusing requirement in order to maximize the sensitivity of our coplanar electrodes and can be enhanced by 10× (measured FWHM = 20 µsec) with particles flowing closer to the streamline center.

To understand the detection limit of our system, we perform measurements on 1- and 0.5-µm polystyrene beads. Before the measurements, the samples are flushed through membrane filters twice to avoid large aggregates. In addition, two adjustments are made in our flow-cytometry system. First, the sensitivity of ILO is adjusted to its maximum by increasing the I_{osc}/I_{inj} ratio (close to the locking edge of the oscillators). This comes at the cost of reduced dynamic range. Second, the sheath flow rate is increased by 4× to focus the beads as close to the surface of the CMOS surface as possible. Though the volume of the polystyrene beads has shrunk by 8,000×, the system can still detect 0.5-µm beads at an SNR > 5, as indicated in Fig. 4(b).

Signal processing

As mentioned in Eq. (1), the measured absolute capacitance values depend on both the size of the cells as well as its elevation in the microfluidic channel. To extract only the frequency-dependent dispersion in cytoplasm permittivity, we employed a self-normalization signal processing technique, which normalizes the high-frequency data (11, 17.5, and 30 GHz) to that of the lowest one (6.5 GHz). This way, both the cell size and the elevation dependency in the measured capacitance is rejected assuming both parameters

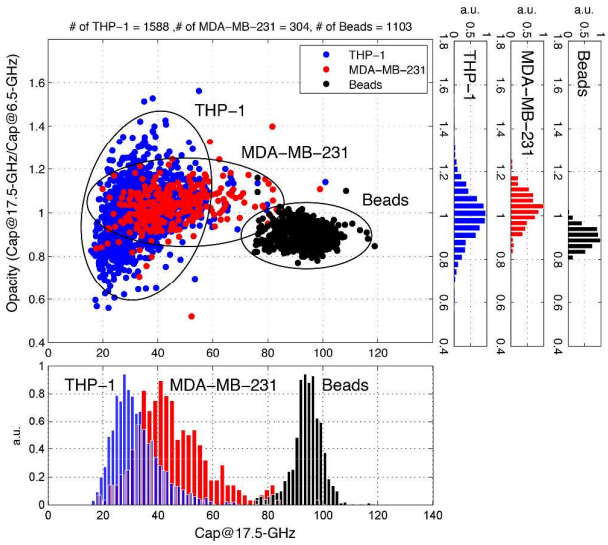

Fig. 5 Measured 2-D scattering plot from leukemia cells (THP-1), breast cells (MDA-MB-231), and 10-µm polystyrene beads. The x-axis shows the measured absolute capacitance. Beads and cells are differentiable. The y-axis plots the opacity, defined as the ratio between the measured capacitance at 17.5 GHz and 6.5 GHz.

remain consistent when flowing across all four sensing channels. This is often termed *opacity*,[15] and hence we will use the same term in this paper. The efficacy of self-normalization is seen in the reduction of distribution spread (1-σ), from 11% to 5% in the polystyrene beads, and from 25% to 11% in the cells experiments, respectively. The residual spread in the polystyrene beads could be attributed to the intrinsic permittivity variation of the polystyrene matrixes, and there is no effective means to perform such type of characterization currently.

Cell-line Measurements

We characterize four different cell lines, two of which belongs to the breast cell lines (MCF-10A and MDA-MB-231) whereas the other two are leukemia cell lines (THP-1 and K-562). The aim of these studies is to understand whether the cell lines exhibit different dispersion in the permittivity at GHz frequencies. Fig. 5 shows a representative 2-D scattering plot (opacity versus absolute capacitance at 17.5 GHz) from THP-1 cells (diameter = 13.9 ± 1.86 µm, mean ± std.), MDA-MB-231 cells (16.5 ± 1.83 µm), and the 10-um polystyrene beads. In the absolute capacitance measurements, the distribution of beads is well separated from those of the cells. In addition, the distributions of THP-1 and MDA-MB-231 exhibit overlapped but different medians and means. On the other hand, the distributions in the dielectric opacity from both cell lines are overlapped with similar mean. These results may infer that the observed distribution difference between the THP-1 and the MDA-MB-231 is mainly due to their size difference, but not the permittivity dispersion. Note that the size for each single cell is not characterized simultaneously in our spectrometer. Therefore this conclusion is made based on ensemble average results.

Next, the two breast cell lines are compared. Fig. 6(a) shows the 2-D scattering plots from the normal (MCF-10A) and cancerous (MDA-MB-231) breast cell lines. First, we notice that MDA-MB-231 exhibits a higher mean capacitance with broader distribution. This is partially due to size difference (16.5 ± 1.83 µm vs. 14.8 ± 2.25 µm). Second, the dielectric opacity at 17.5 GHz exhibits a noticeable difference in its distribution whereas significant overlapping is observed at 11 and 30 GHz. Summarized results from Fig. 7 indicates that these two cell lines exhibit different permittivity dispersion around 17.5 GHz. In particular, the opacity of the two cell lines exhibits opposite trends when the measurement frequency increases from 11 to 17.5 GHz. As the measured capacitance represents the dielectric contrast against the medium, the results indicate that MDA-MB-231 exhibits a faster roll-off in its permittivity with increasing frequency between 11 and 30 GHz when comparing with MCF-10A.

We also compare the two leukemia cell lines with summarized results shown in Fig. 7. In this case, no significant difference in the opacity is observed, except minor separation in the distribution of the absolute measured capacitance due to their sizes (13.9 ± 1.86 µm vs. 14.9 ± 1.9 µm, mean ± std.). These indicate that the THP-1 (monocytes from acute monocytic leukemia) and K-562 (lymphoblasts from chronic myelogenous leukemia) exhibit similar dispersion in their cytoplasm permittivity.

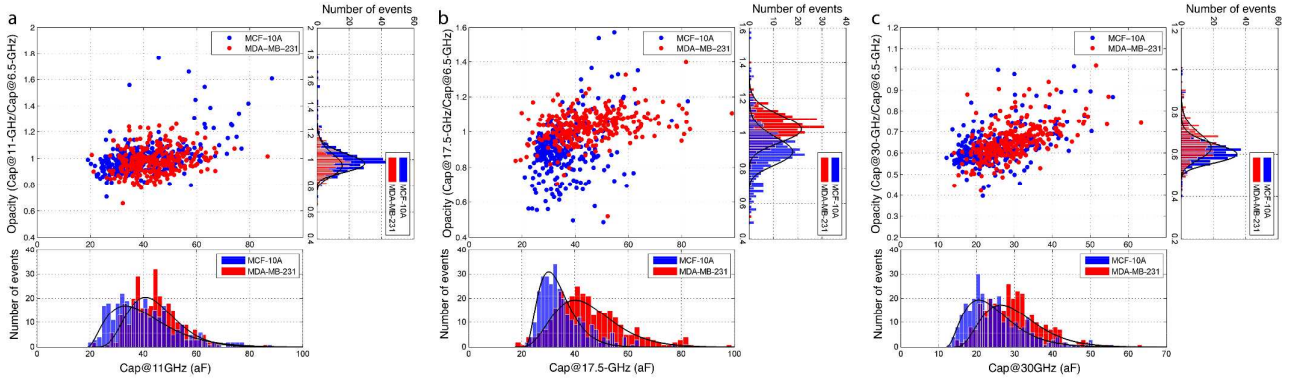

Fig. 6 Measured scattering plot from two breast cell lines (MCF-10A and MDA-MB-231) at (a) 11, (b) 17.5, and (c) 30 GHz. The distributions are fitted using Gamma function. It is seen that the MDA-MB-231 cells exhibit larger average cell size and broader distribution. The opacity at 17.5 GHz exhibits separable distribution as compared to 11- and 30-GHz data. Number of samples >= 303.

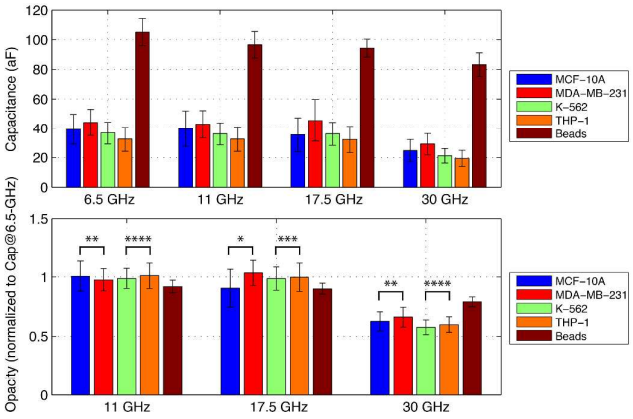

Fig. 7 Measurements of four cell lines (MCF-10A, MDA-MB-231, THP-1, and K-562) with polystyrene beads: (a) absolute mean capacitance and (b) mean dielectric opacity. The error bar represents one standard deviation. The median exhibits similar trends with an offset value. In the dielectric opacity, the MDA-MB-231 cells exhibit larger mean signal level than MCF-10A cells at 17.5 GHz. This implies that the MDA-MB-231 cells exhibit larger relaxation time constant, leading to early roll-off in its permittivity when increasing the frequencies. Number of samples in MCF-10A and MDA-MB-231 cell measurements >= 303, *: two-sample t-test with unequal variance with p << 0.00001, **: two-sample t-test with unequal variance with p = 0.001. Number of samples in K-562 and THP-1 cell measurements >= 1588, ***: two-sample t-test with unequal variance with p = 0.003, ****: two-sample t-test with unequal variance with p << 0.001.

Conclusions and outlook

We present a sub-aF resolution CMOS/Microfluidics microwave flow cytometry for single-cell dielectric spectroscopy, sampling cytoplasm permittivity at 6.5, 11, 17.5, and 30 GHz. This is achieved by the proposed electronic architecture using on-chip injection-locked LC-oscillators embedded in an interferometry for optimal noise cancellation and low-cost mass-producible CMOS/microfluidic integration. Compared to Zheng et. al.[35], the presented GHz measurement platform not only offers higher sensitivity but also enables the capture of cell-specific dielectric spectrum instead of averaging over multiple cells in a compact instrumentation form factor. Benefitting from the flow, a large number of cells can be quantified in a relatively short amount of time without labor-intensive protocols. These advancements enable quantification of cellular fingerprints at GHz. The proposed epoxy-injection process also simplifies the interfacing of millimeter-size CMOS chip and centimeter-size microfluidics while preserving large microfluidics working area. This step not only protects the biological cells from the toxic PCB surface but also avoids the need of custom lithography processes for creating an electrical connection, making the packaging flow well suited for future low-cost mass-produced **"**lab-on-CMOS**"** platform.

Measurements in breast cell lines at large scale show that there is indeed a difference in *average* frequency-dependent permittivity between normal (MCF-10A) and highly metastatic cancer cell lines (MDA-MB-231) across 6.5 – 30 GHz. Here we hypothesize that such a difference could be due to more randomized ordering in local mass density within the cytoplasm and nucleus of the highly metastatic cancerous cells, as this is one of the largest physical difference observed in MCF-10A and MDA-MB-231 cell lines using partial wave spectroscopy (PWS)[68] and its variant, the quantitative phase imaging (QPI).[69] The non-uniformed local mass density can infer clustered structure in the cytoskeleton, which can attribute to the changes in the distribution of the dielectric relaxation according to the Effective Medium Theory (EMT).[28,70] Though the concept is proposed for the first time, comprehensive model validation requires future work to integrate multi-modality, such as dielectric spectroscopy and PWS, for correlation studies. Measurement protocols should also include real-time monitoring of the changes in both the biophysical and physiological states of the cells. In addition, since cytoskeleton integrity infers cellular stiffness (or deformability under applied stress),[71] it is of interest to study the correlation between cellular electrical and mechanical biomarkers. Our CMOS dielectric spectrometer should also be equipped with higher sampling capability (currently only four frequencies is included in our measurements) to increase the resolution in quantifying the relaxation process across the bandwidth of interest. It is also informative to push the frequencies above 30 GHz, perhaps toward sub-THz frequencies for new fingerprint discovery. These additional data will not only facilitate the capture of the dielectric spectroscopic dispersion for each cell line but also enable the use of signal processing techniques such as principal component analysis for feature extraction and discrimination.

Last, we believe our GHz-sensing platform can be adapted and integrated for various applications given its low limit-of-detection and physical-based sensing mechanism. Aside from simple cell counting[17,18], our system can be adapted for droplets measurements[72], electrophoresis(DEP)-based cytometry[47], and to work similarly as electrical impedance spectroscopy (EIS) for label-free molecular sensing for glucose,[73] DNA,[74] and protein conformation.[50] Given the capability of integrating multi-parametric detection electronics in a single CMOS chip,[75] we believe such a "Lab-on-CMOS" platform will find a new opportunity for future point-of-care applications.

Conflicts of interest

The authors confirm that there are no conflicts to declare.

Author Contributions

J.-C.C. and A.M.N developed the research project. J.-C.C. proposed the CMOS spectrometer design and microfluidics integration technique. J.-C.C. and A.A. performed the experiments. A.N.K. prepared the cell lines. All the authors contributed to the manuscript writing.

Acknowledgements

The authors would like to acknowledge TSMC University Shuttle Program for chip fabrication, Integrand Inc. for the support of EMX, Chih-Ming Lin, Yang Lin, Yenhao Philip Chen, Ruonan Liu, and Wei-Cheng Li of Berkeley Sensor and Actuator Center (BSAC) for various discussions, and Paul Lum

from Biomolecular Nanotechnology Center (BNC) at Berkeley, for the experiment supports.

References

1 D. R. Gossett, W. M. Weaver, A. J. Mach, S. C. Hur, H. T. K. Tse, W. Lee, H. Amini, D. Di Carlo, *Anal. Bioanal. Chem.*, 2010, **397**, 3249.
2 Y. Zheng, J. Nguyen, Y. Wei, Y. Sun, *Lab Chip*, 2013, **13**, 2464.
3 C. Wyatt Shields IV, C. D. Reyes, G. P. Lopez, *Lab Chip*, 2015, **15**, 1230.
4 E. M. Hansson, M. E. Lindsay, K. R. Chien, *Cell Stem Cell*, 2009, **5**, 364.
5 F. B. Myers, C. K. Zarins, O. J. Abilez, L. P. Lee, *Lab Chip*, 2013, **13**, 220.
6 S. Gawad, L. Schild, P. Renaud, *Lab Chip*, 2001, **1**, 76.
7 S. Gawad, K. Cheung, U. Seger, A. Bortsch, P. Renaud, *Lab Chip*, 2004, **4**, 241.
8 K. Cheung, S. Gawad, P. Renaud, *Cytometry Part A*, 2005, **65(2)**, 124.
9 H. Morgan, T. Sun, D. Holmes, S. Gawad, N. G. Green, *J. Phys. D: Appl. Phys.*, 2007, **40**, 61.
10 T. Sun, H. Morgan, *Microfluid. Nanofluid.*, 2010, **8**, 423.
11 C. Petchakup, K. H. H. Li, and H. W. Hou, *Micromachines*, 2017, **8(3)**, 87.
12 N. Haandbæk, S. C. Burgel, F. Heer, A. Hierlemann, *Lab Chip*, 2014, **14**, 369.
13 N. Haandbæk, S. C. Burgel, F. Rudolf, F. Heer, A. Hierlemann, *ACS Sensors*, 2016, **1(8)**, 1020.
14 D. Holmes, H. Morgan, *Anal. Chem*., 2010, **82**, 1455.
15 D. Holmes, D. Pettigrew, C. H. Reccius, J. D. Gwyer, C. van Berkel, J. Holloway, D. E. Davies, H. Morgan, *Lab Chip* 2009, **9**, 2881.
16 C. van Berkel, J. D. Gwyer, S. Deane, N. Green, J. Holloway, V. Hollis, H. Morgan, *Lab Chip*, 2011, **11**, 1249.
17 N. N. Watkins, U. Hassan, G. Damhorst, H. Ni, A. Vaid, W. Rodriguez, R. Bashir, *Sci. Transl. Med.,* 2013, **5(214)**, 214ra170.
18 U. Hassan, T. Ghonge, B. Reddy Jr., M. Patel, M. Rappleye, I. Taneja, A. Tanna, R. Healey, N. Manusry, Z. Price, T. Jensen, J. Berger, A. Hasnain, E. Flaugher, S. Liu, B. Davis, J. Kumar, K. White, R. Bashir, *Nature Comm*., 2017, **8**, 15949.
19 Y. Zheng, J. Nguyen, C. Wang, and Y. Sun, *Lab Chip*, 2013, **13**, 3275.
20 K. Wang, Y. Zhao, D. Chen, B. Fan, Y. Lu, L. Chen, R. Long, J. Wang, J. Chen, *Sci. Data*, 2017, **4**, 170015.
21 Y. Zhao, M. Jiang, D. Chen, X. Zhao, C. Xue, R. Hao, W. Yue, J. Wang, J. Chen, *Sci. Reports*, 2016, **6**, 19487.
22 T.-K. Chiu, Y. Zhao, D. Chen, C.-H. Hsieh, K. Wang, W.-P. Chou, C.-J. Liao, H.-Y. Wang, B. Fan, J. Wang, J. Chen, M.-H. Wu, *Sensors and Actuators B: Chemical*, 2017, **246**, 29.
23 D. Spencer, V. Hollis, and H. Morgan, *Biomicrofluidics*, 2014, **8**, 064124.
24 H. Song, Y. Wang, J. M. Rosano, B. Prabhakarpandian, C. Garson, K. Pant, E. Lai, *Lab Chip*, 2013, **13**, 2300.
25 Y. Zhao, Q. Liu, H. Sun, D. Chen, Z. Li, B. Fan, J. George, C. Xue, Z. Cui, J. Wang, J. Chen, *PLoS One*, 2016, **11(6)**, e0518044.
26 K. Grenier, D. Dubuc, T. Chen, F. Artis, T. Chrétiennot, M. Poupon, J.-J. Fournié, *IEEE Trans. Microw. Theory Tech.*, 2013, **61(5)**, 2023.
27 F. Artis, T. Chen, T. Chrétiennot, J.-J. Fournié, M. Poupon, D. Dubuc, K. Grenier, *Microwave Magazine*, 2015,**16(4)**, 87.
28 K. Asami, *Porg. Polym. Sci.*, 2002, **27**, 1617.
29 K. Grenier, D. Dubuc, P.-E. Poleni, M. Kumemura, H. Toshiyoshi, T. Fuji, H. Fujita, *IEEE Trans. Microw. Theory Tech.*, 2009, **57(12)**, 3246.
30 T. Chen, F. Artis, D. Dubuc, J.-J. Fournier, M. Poupon, K. Grenier, *IEEE MTT-S Inter. Microw. Sym.*, 2013.
31 A. Zedek, D. Dubuc, K. Grenier, *IEEE MTT-S Inter. Microw. Sym.*, 2017.
32 A. Tamra, D. Dubuc, M.-P. Roll, K. Grenier, *IEEE Trans. Microw. Theory Tech.*, 2017, **65(9)**, 3512.
33 Y. Ning, C. Multari, X. Luo, C. Paleo, X. Cheng, J. C. M. Hwang, A. Renzi, C. Merla, F. Apollonia, M. Liberty, *IEEE Trans. Microw. Theory Tech.*, 2014, **62(9)**, 1905.
34 Y. Yang, H. Zhang, J. Zhu, G. Wang, T.-R. Tseng, X. Xuan, K. Huang, P. Wang, *Lab Chip*, 2010, **10**, 553.
35 L. Y. Zhang, C. Bounaix Morand du Puch, C. Dalmay, A. Lacroix, A. Landoulsi, J. Leroy, C. Mélin, F. Lalloué, S. Battu, C. Laurette, S. Giraud, A. Bessaudou, P. Blondy, M. O. Jauberteau, A. Pothier, *Sensors and Actuators A: Physical*, 2014, **216**, 405.
36 N. Haandbæk, O. With, S. C. Burgel, F. Heer, A. Hierlemann, *Lab Chip*, 2014, **14**, 3313.
37 X. Ma, N. D. Orloff, C. A. E. Little, C. J. Long, I. E. Hanemann, S. Liu, J. Mateu, J. C. Booth, J. C. M. Hwang, *IEEE Trans. Microw. Theory Tech.*, 2018, **66(2)**, 1099.
38 K. Entesari, A. A. Helmy, M. Moslehi-Bajestan, *IEEE Microwave Magazine*, 2017, **18(5)**, 57.
39 M. Moslehi-Bajestan, A. A. Helmy, H. Hedayat, K. Entesari, *IEEE Trans. Microw. Theory Tech.*, 2014, **62(12)**, 3522.
40 A. A. Helmy, H.-J. Jeon, Y.-C. Lo, A. J. Larsson, R. Kulkarni, J. Kim, J. Silva-Martinez, K. Entesari, *IEEE J. of Solid-State Circuits*, 2012, **47(10)**, 2467.
41 G. Guarin, M. Hofmann, J. Nehring, R. Weigel, G. Fischer, D. Kissinger, *IEEE Microwave Magazine*, 2015, **16(4)**, 71.
42 F. I. Jamal, S. Guha, M. H. Eissa, J. Borngräber, C. Melanie, H. J. Ng, D. Kissinger, J. Wessel, *IEEE Trans. Microw. Theory Tech.*, 2017, **65(3)**, 1012.
43 T. Mitsunaka, D. Sato, N. Ishida, A. Saito, K. Iizuka, T. Suzuki, Y. Ozawa, M. Fujishima, *IEEE J. of Solid-State Circuits*, 2016, **5(11)**, 2534.
44 M. Bakhshiani, M. A. Suster, P. Mohseni, *IEEE Trans. on Biomedical Circuits and Systems*, 2015, **9(6)**, 849.
45 J.-C. Chien, M. Anwar, E.-C. Yeh, L. P. Lee, A. M. Niknejad, *IEEE MTT-S Inter. Microw. Sym.,* 2013.
46 K. Mohammad, D. A. Buchanan, K. Braasch, M. Butler, D. J. Thomson, *Sensors and Actuators B: Chemical*, 2017, **249**, 246.
47 G. A. Ferrier, S. F. Romanuik, D. J. Thomson, G. E. Bridges, and M. R. Freeman, *Lab Chip*, 2009, **9**, 3046.
48 M. Nikoolic-Jaric, S. F. Romanuik, G. A. Ferrier, G. E. Bridges, M. Butler, K. Sunley, D. J. Thomson, M. R. Freeman, *Biomicrofluidics*, 2009, **3**, 034103.
49 J.-C. Chien, A. M. Niknejad, *IEEE J. of Solid-State Circuits*, 2016, **51(2)**, 457.
50 J.-C. Chien, A. M. Niknejad, *IEEE J. of Solid-State Circuits*, 2016, **51(8)**, 1851.
51 H. Lee, Y. Liu, R. M. Westervelt, D. Ham, *IEEE J. of Solid-State Circuits,* 2006, **41(6)**, 1471.
52 H. Lee, Y. Liu, D. Ham, and R. M. Westervelt, *Lab Chip*, 2007, **7**, 331.
53 A. Uddin, K. Milaninia, C.-H. Chen, L. Theogarajan, *IEEE Trans Compon. Packaging Manuf. Technol.*, 2011, **1(12)**, 1996.
54 Y. Huang, A. J. Mason, *Lab Chip*, 2013, **13**, 3929.
55 D. Welch, J. B. Christen. *J. Micromech. and Microeng*., 2013, **23**, 035009.
56 T. Datta-Chaudhuri, P. Abshire, E. Smela, *Lab Chip*, 2014, **14**, 1753.
57 T. Datta-Chaudhuri, E. Smela, P. A. Abshire, *IEEE Trans. Biomedical Circuits and Systems*, 2016, **10(6)**, 1129.
58 M. Inac, M. Wietstruck, A. Göritz, B. Cetindogan, C. Baristiran-Kaynak, S. Marschmeyer, M. Fraschke, T. Voss, A. Mai, C. Polego, A. Pothier, M. Kaynak, *IEEE Electronic Compon. and Tech. Conf.*, 2017.
59 E. Ghafar-Zadeh, M. Sawan, D. Therriault, S. Rajagopalan, V. P. Chodavarapu, *Microelectronic Engineering*, 2009, **86**, 2104.
60 A. Wu, L. Wang, E. Jensen, R. Mathies, B. Boser, *Lab Chip*, 2010, **10**, 519.
61 V. Iyer, P. Murali, J. Paredes, D. Liepmann, B. Boser, *Transducer*, 2015, 1822.

62 M. Muluneh, D. Issadore, *Lab Chip*, 2014, **14**, 4552.
63 J.-C. Chien, E.-C. Yeh, L. P. Lee, M. Anwar, A. M. Niknejad, *IEEE MTT-S Inter. Microw. Sym.,* 2014.
64 B. Zhang, Q. Dong, C. E. Korman, Z. Li, M. E. Zaghloul, *Sci. Reports*, 2013, **3**, 1098.
65 H. Wang, A. Mahdavi, D. A. Terrell, A. Hajimiri, *Lab Chip*, 2012, **12**, 4464.
66 C. Simonet, A. Groisman, *Appl. Phys. Lett*., 2005, **87**, 114104.
67 D. S. Kim, D. S. Kim, K. Han, W. Yang, *Microelectronic Engineering*, 2009, **86**, 1343.
68 D. B. Agus, et. al., *Sci. Reports*, 2013, **3**, 1449.
69 W. J. Eldridge, Z. A. Steelman, B. Loomis, A. Wax, *Biophysical Journal*, 2017, **112**, 692.
70 K. Heinemann, J. Daoud, M. Tabrizian, *Biosensors and Bioelectronics*, 2013, **49**, 348.
71 D. R. Gossett, H. T. K. Tse, S. A. Lee, Y. Ying, A. G. Lindgren, O. O. Yang, J. Rao, A. T. Clark, D. Di Carlo, *Proc. Natl. Acad. Sci.*, 2012, **109(20)**, 7630.
72 G. Yesiloz, M. S. Bombay, C. L. Ren, *Lab Chip*, 2015, **15**, 4008.
73 J.-C. Chien, E.-C. Yeh, L. P. Lee, M. Anwar, and A. M. Niknejad, *IEEE MTT-S Inter. Microw. Sym.,* 2015.
74 K. M. Taylor, D. W. van der Weide, *IEEE Trans. Microw. Theory Tech.*, 2005, **53(5)**, 1576.
75 Y.-J. Huang, T.-H. Tseng, T.-W. Lin, C.-W. Huang, P.-W. Yen, P.-H. Kuo, C.-T. Lin, S.-S. Lu, *IEEE J. of Solid-State Circuits*, 2014, **49(4)**, 851.

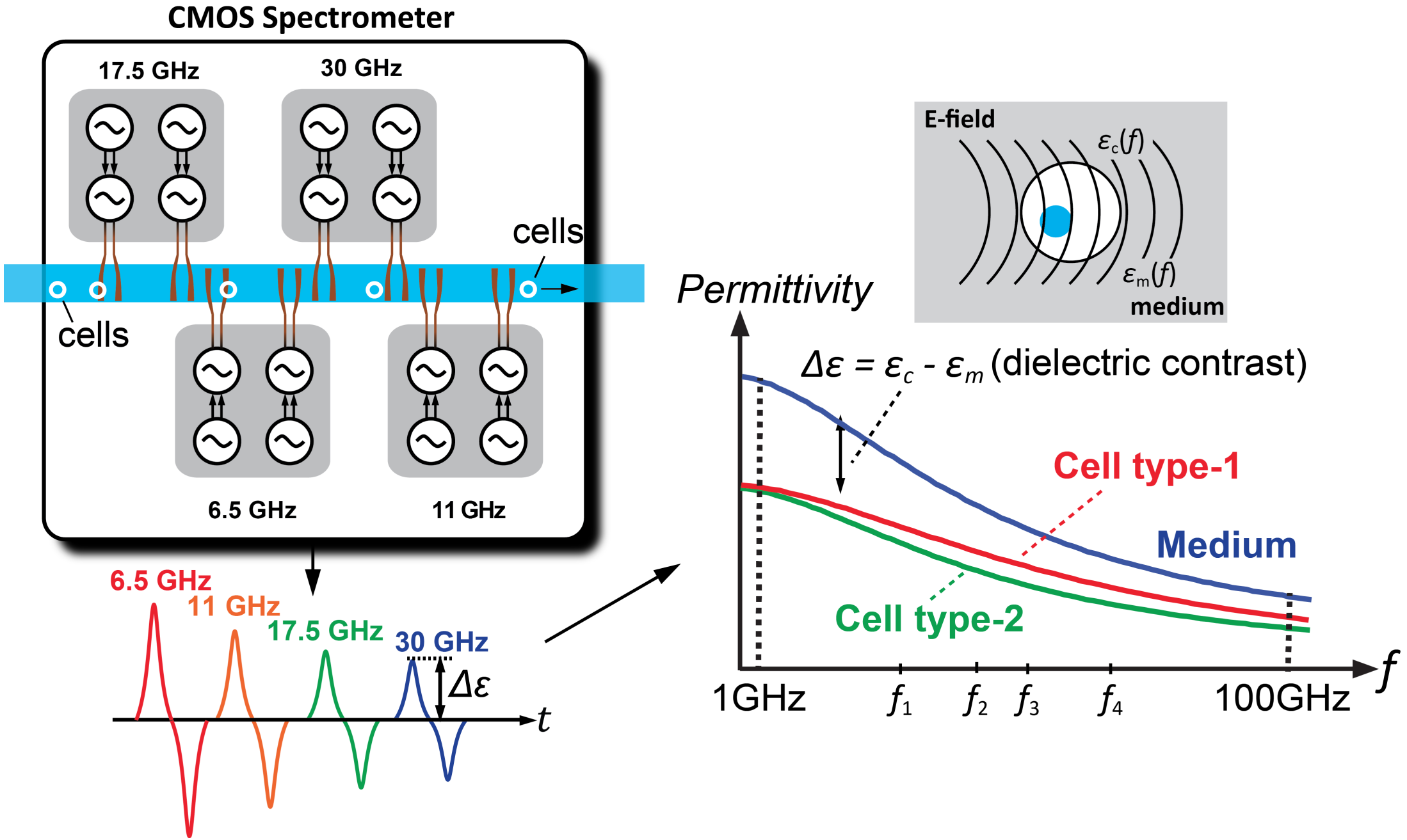
CMOS Spectrometer
17.5 GHz
30 GHz
cells
cells
6.5 GHz
11 GHz
6.5 GHz
11 GHz
17.5 GHz
30 GHz
Δε
t
E-field
εc(f)
εm(f)
medium
Permittivity
Δε = εc - εm (dielectric contrast)
Cell type-1
Medium
Cell type-2
1GHz
f1
f2
f3
f4
100GHz
f